Multi-Dimensional Incoherent Thomson Scattering System in PHASMA

Peiyun Shi[a] and Earl E. Scime[b]
Department of Physics and Astronomy, West Virginia University and Center for KINETIC Plasma Physics, Morgantown, WV 26506, USA

An multi-dimensional incoherent Thomson scattering diagnostic system capable of measuring electron temperature anisotropies at the level of the electron velocity distribution function (EVDF) is implemented on the PHAse Space MAppgin (PHASMA) facility to investigate electron energization mechanisms during magnetic reconnection. This system incorporates two injection paths (perpendicular and parallel to the axial magnetic field) and two collection paths, providing four independent EVDF measurements along four velocity space directions. For strongly-magnetized electrons, a 3D EVDF comprised of two characteristic electron temperatures perpendicular and parallel to the local magnetic field line is reconstructed from the four measured EVDFs. Validation measurements of isotropic electrons in a single magnetic flux rope and a steady-state helicon plasma is presented.

I. INTRODUCTION

Electrons in weakly-collisional or collisionless plasma systems are usually in a non-equilibrium state. Not only are the electrons not in thermal equilibrium with ions and other species, but their own ensemble has not relaxed to local thermodynamic equilibrium.[1] Thus, kinetic descriptions of electrons, i.e. complete description of the electron velocity distribution function (EVDFs) $F_e(v_x, v_y, v_z)$, reveal physics beyond the assumptions of magnetohydrodynamics.[2,3] Two important non-equilibrium features easily identified in EVDF measurements are deviations from a Maxwellian velocity distribution and the electron temperature anisotropy (different electron temperatures along different velocity directions).

An example of this non-equilibrium system is the solar wind, where electron temperature anisotropy is constrained by anisotropy-induced kinetic instabilities and Coulomb collisions.[4] In the magnetosphere, magnetic reconnection[5,6] and wave-particle interactions[7] energize electrons selectively and the EVDFs exhibit clear non-Maxwellian features. In laboratory plasmas, including low-temperature weakly ionized plasmas,[8] non-Maxwellian or anisotropic electrons are generated by weak collisions,[9] strong electric fields,[10] and external energy inputs that target specific portions of the EVDF.[11] Therefore, the ability to diagnose EVDFs in multi-dimensional velocity phase space is essential for investigating physics mechanisms that result in non-equilibrium EVDFs.[2,12]

Langmuir probes[13] and various retarding field energy analyzers[14] are often used to indirectly measure EVDFs. However, it is difficult, if not impossible, to improve their spatial resolution to electron kinetic scales (sub gyroradius scales) and their perturbative effects on the EVDFs themselves are nearly impossible to quantify. Passive spectroscopy techniques using visible light[15] and soft X-rays[16] can provide non-perturbative EVDF measurements, though integrated along a line of sight. These limitations are overcome with active spectroscopic diagnostics, *e.g.*, Thomson scattering. Thomson scattering is capable of measuring spatially-resolved EVDFs along specific velocity directions at the kinetic scale. Recently, several Thomson scattering systems have been implemented in basic plasma facilities[17–20] to probe non-equilibrium electrons. However, EVDFs along only one velocity direction (two at most) are measured in most experiments. Such measurements are insufficient to quantify electron temperature anisotropy. Interestingly, Milder *et al.*[21] developed an angular resolved coherent Thomson scattering system, which provided spectra along multiple velocity directions. But no anisotropy measurements were obtained from that system because electron temperature isotropy has to be assumed as part of the measurement process to remove the requirement of *a priori* knowledge of the EVDF.

Here we describe a unique, multi-dimensional incoherent Thomson scattering system installed on the PHAse Space MApping (PHASMA) facility. In Sec. II, the experimental configuration including the arrangements of two injection and two collection optical paths and the method to reconstruct 3D EVDFs are presented. Preliminary multi-dimensional EVDFs measured in pulsed magnetic flux ropes and static helicon plasmas are presented in Sec. III. A brief summary is given in Sec. IV.

II. EXPERIMENTAL APPARATUS

PHASMA is a basic plasma experimental facility at West Virginia University built to investigate electron and ion energization in magnetized plasmas.[22] As shown in Fig. 1, PHASMA is a linear device equipped with two plasma sources (a pair of pulsed plasma guns and a steady-state helicon source). Ongoing studies in PHASMA include investigations of magnetic reconnection[9] and waves and turbulence.[23] A novel feature of PHASMA is its comprehensive suite of laser-based, particle diagnostics, *e.g.*, incoherent Thomson scattering,[17] laser induced fluorescence,[24] and Zeeman splitting.[25] These diagnostics are used to non-perturbatively measure EVDFs, ion velocity distribution functions (IVDFs) and magnetic fields. Originally only able to measure EVDFs in 1D velocity space,[17] the incoherent Thomson scattering system has been upgraded to enable measurements of EVDFs in multi-dimensional velocity space.

[a]Author to whom correspondence should be addressed: peiyun.shi@mail.wvu.edu
[b]Author to whom correspondence should be addressed: earl.scime@mail.wvu.edu

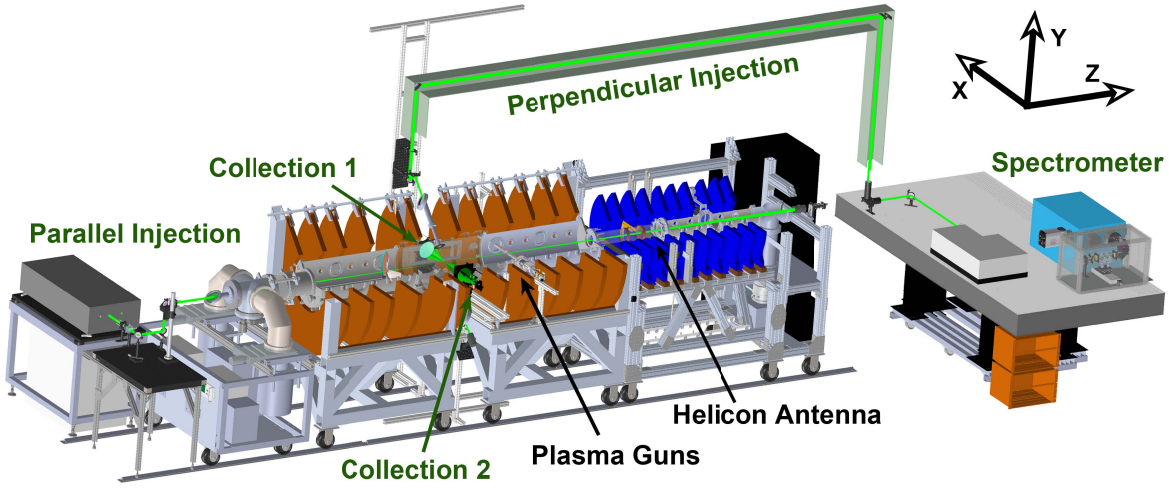

FIG. 1. Experimental layout of the multi-dimensional incoherent Thomson scattering system on the PHASMA facility. It includes two injections along perpendicular and parallel (to z) directions and two collection paths 1 and 2. Two types of plasma sources, plasma guns and helicon antenna, are used to generate plasmas to benchmark this diagnostic.

Two injection paths and two collection paths are employed to provide four Thomson scattering spectra along different velocity directions to reconstruct multi-dimensional EVDFs. For the perpendicular injection path, one Quantel pulsed Nd:YAG laser at the second harmonic wavelength $\lambda_i = 532$ nm serves as a source of 450 mJ/pulse light. After one beam expander and six mirrors in the beam line, the incident light is focused into the target chamber along $\mathbf{k_{i\perp}}$, $\theta = -135^\circ$ in xy plane, with the polarization direction along z. Another Quanta-Ray pulsed Nd:YAG laser also at 532 nm and with a nominal energy 600 mJ/pulse is used for parallel (to the background magnetic field) light injection along $\mathbf{k_{i\parallel}}$. One beam expander and three mirrors transmit laser light into the vacuum chamber along z with the polarization direction along y through a Brewster window at the end of PHASMA and a hole in the apex of the conical anode on which the plasmsa gun discharges terminate.

Two collection paths with wavevectors $\mathbf{k_{s1}}$ and $\mathbf{k_{s2}}$ lie along $+x$ and $-x$, respectively. Each collection optics assembly includes one 150-mm diameter convex lens of focal length 150 mm, one rotatable linear polarizer in front of a linear fiber bundle containing 30 single fibers with a format of 3×10. The two sets of fiber bundles conveying light from the collection paths 1 and 2 are combined into a single fiber bundle with a format of 1×60 at the exit end of the fibers. The 1×60 fiber bundle is aligned vertically at the entrance slit of the spectrometer. Spectra from the two collection paths then appear at different heights on the spectrometer camera, enabling the acquisition of spectra from both collection paths without needing to adjust injection optics into the spectrometer.

In between the exit face of the collection fiber bundles and the entrance slit of the spectrometer, two volume Bragg gratings[26] are inserted in series as a notch filter to suppress stray light at 532 nm. The 670-mm Czerny-Turner spectrometer, equipped with a 1200-groove/mm grating, disperses collected light in wavelength space and the dispersed light is detected with an intensified CCD (iCCD). A Gen-III image intensifier is used for this iCCD for its higher quantum efficiency $> 47\%$ at 532 nm. In addition to the Brewster windows mounted on the chamber and the polarizers in the collection optic assemblies, other measures are employed to suppress stray light from the incident laser (since its intensity is $10^{14}\times$ the expected intensity of the scattered photons). These measures include irises and planar baffles in the flight tubes, beam dumps at the laser exit side, and a short gate time window for the iCCD.[17]

Figure 2(a) summarizes the layout of wavevectors in the present system, including two the injection paths, $\mathbf{k_{i\perp}}$ and $\mathbf{k_{i\parallel}}$, and the two collection paths $\mathbf{k_{s1}}$ and $\mathbf{k_{s2}}$. Four Thomson scattering spectra are obtained at a specific time and location along four different velocity directions, i.e., the four differential scattering wavevectors $\mathbf{k_{\perp 1}} = \mathbf{k_{s1}} - \mathbf{k_{i\perp}}$ (gray), $\mathbf{k_{\perp 2}} = \mathbf{k_{s2}} - \mathbf{k_{i\perp}}$ (blue), $\mathbf{k_{\parallel 1}} = \mathbf{k_{s1}} - \mathbf{k_{i\parallel}}$ (magenta) and $\mathbf{k_{\parallel 2}} = \mathbf{k_{s2}} - \mathbf{k_{i\parallel}}$ (red).[27] These wavevectors are projected on xy and xz planes in Fig. 2(b) and (c), showing the corresponding scattering angles $\theta_{s\perp 1} = 135^\circ$, $\theta_{s\perp 2} = 45^\circ$, $\theta_{s\parallel 1} = 90^\circ$ and $\theta_{s\parallel 2} = 90^\circ$. Note that values of the four scattering parameters are $\alpha_{\perp 1} = \lambda_i/[4\pi \sin(\theta_{s\perp 1}/2)\lambda_D] = 0.011$, $\alpha_{\perp 2} = 0.027$, $\alpha_{\parallel 1} = 0.015$, and $\alpha_{\parallel 2} = 0.015$, where λ_D is the Debye length. The values of α guarantee that all four measured spectra $f_e(\lambda_{k\perp 1})$, $f_e(\lambda_{k\perp 2})$, $f_e(\lambda_{k\parallel 1})$ and $f_e(\lambda_{k\parallel 2})$ are in the incoherent regime,[27] though with different magnitudes for each of the scattering wavevectors.

The 3D EVDFs $F_e(v_x, v_y, v_z)$ are obtained by measuring four 1D EVDFs and accounting for other physical constraints of the experiment. The electrons are strongly magnetized by the axial magnetic field, i.e., electron gyroradius ~ 0.1 mm and gyroperiod ~ 1 ns are smaller than both the characteristic spatial and time scales of most interesting plasma processes and the spatial and temporal resolutions of this Thomson scattering system. The electron temperature in the perpendicular xy plane is expected to be isotropic (gyrotropic). Thermal anisotropy, if it exists, will be between the parallel

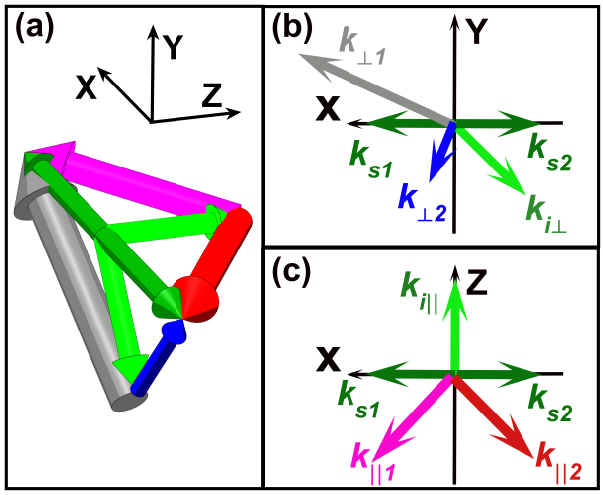

FIG. 2. (a) The measurement wavevectors for the multi-dimensional Thomson scattering system (b) projected into the 2D xy plane and the (c) xz plane. Perpendicular $\mathbf{k_{i\perp}}$ and parallel $\mathbf{k_{i\parallel}}$ injection wavevectors are in green and the two collection wavevectors $\mathbf{k_{s1}}$ and $\mathbf{k_{s2}}$ are in olive. The measured EVDFs are along four differential scattering wavevectors, $\mathbf{k}_{\perp\mathbf{1}}$ (gray), $\mathbf{k}_{\perp\mathbf{2}}$ (blue), $\mathbf{k}_{\parallel\mathbf{1}}$ (magenta) and $\mathbf{k}_{\parallel\mathbf{2}}$ (red).

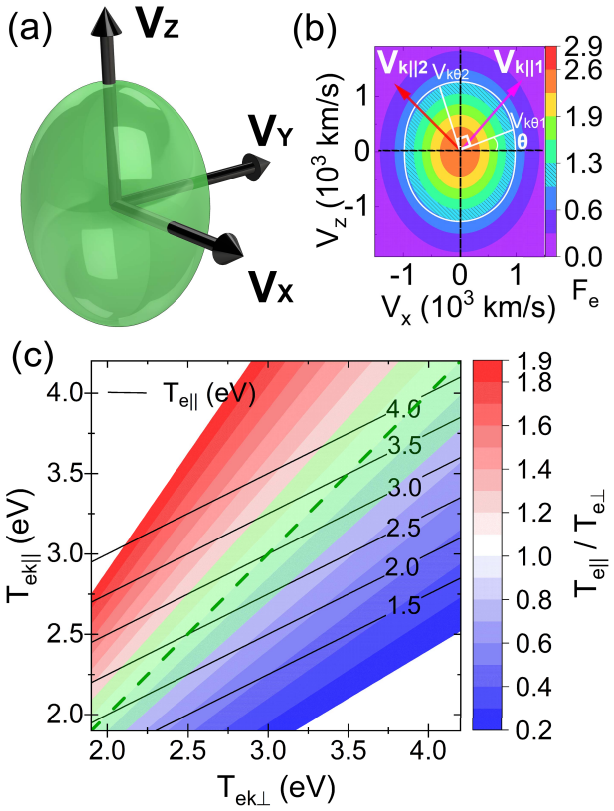

FIG. 3. (a) A 3D EVDF for a distribution with anisotropic parallel and perpendicular electron temperatures. (b) The projected 2D EVDF on the v_x-v_z plane. The two white straight lines show the new orthogonal coordinate $v_{k\theta 1}$-$v_{k\theta 2}$, offset from v_x-v_z by θ. The calculated thermal electron velocity of $f_e(V_{k\theta 1})$ is plotted as the white curved line. Magenta and red arrows denote velocity directions $V_{k||1}$ and $V_{k||2}$ of measured EVDFs $f_e(v_{k||1})$ and $f_e(v_{k||2})$. (c) The parallel electron temperature $T_{e||}$ (contour lines) and electron temperature anisotropy $T_{e||}/T_{e\perp}$ as a function of $T_{ek\perp}$ and $T_{ek||}$. The green shaded region around the dashed line represents isotropic electrons considering 10% measurement uncertainty.

($T_{e||}$) and perpendicular ($T_{e\perp}$) directions. Figure 3(a) shows $F_e(v_x,v_y,v_z) = \frac{1}{\pi V_{te\perp}^2}\frac{1}{\sqrt{\pi}V_{te||}}\exp\left(-\frac{v_x^2+v_y^2}{V_{te\perp}^2}-\frac{v_z^2}{V_{te||}^2}\right)$, where $V_{te\perp}$ and $V_{te||}$ are electron thermal velocities corresponding to $T_{e\perp}$ and $T_{e||}$.

The measured $T_{ek\perp 1}$ and $T_{ek\perp 2}$ from EVDFs $f_e(\lambda_{k\perp 1})$ and $f_e(\lambda_{k\perp 2})$ depend explicitly on $T_{e\perp}$,

$$T_{e\perp} = T_{ek\perp 1,2}. \tag{1}$$

However, $T_{ek||1}$ and $T_{ek||2}$, which are obtained from $f_e(\lambda_{k||1})$,and $f_e(\lambda_{k||2})$, contain information from both $T_{e\perp}$ and $T_{e||}$. As is shown by the color contours in Fig. 3(b), the EVDFs projected on the 2D v_x-v_z plane: $F_e(v_x,v_z) = \int dv_y F_e(v_x,v_y,v_z) = \frac{1}{\sqrt{\pi}V_{te\perp}}\frac{1}{\sqrt{\pi}V_{te||}}\exp\left(-\frac{v_x^2}{V_{te\perp}^2}-\frac{v_z^2}{V_{te||}^2}\right)$. To derive the electron temperature $T_{ek\theta 1}$ along the velocity direction $v_{\theta 1}$, offset from v_x by θ, we represent $F_e(v_x,v_z)$ in the new orthogonal coordinate $v_{k\theta 1}$-$v_{k\theta 2}$, $F_e(v_{k\theta 1},v_{k\theta 2}) = \frac{1}{\sqrt{\pi}V_{te\perp}}\frac{1}{\sqrt{\pi}V_{te||}}\exp\left[-\frac{(v_{k\theta 1}\cos\theta - v_{k\theta 2}\sin\theta)^2}{V_{te\perp}^2}-\frac{(v_{k\theta 1}\sin\theta + v_{k\theta 2}\cos\theta)^2}{V_{te||}^2}\right]$. Then, the 1D EVDF becomes

$$f_e(v_{k\theta 1}) = \int dv_{k\theta 2} F_e(v_{k\theta 1},v_{k\theta 2}) = \frac{1}{\sqrt{\cos^2\theta V_{te\perp}^2 + \sin^2\theta V_{te||}^2}} \times \frac{1}{\sqrt{\pi}}\exp\left[-\frac{v_{k\theta 1}^2}{\cos^2\theta V_{te\perp}^2 + \sin^2\theta V_{te||}^2}\right]. \tag{2}$$

For a bi-Maxwellian (two temperature) EVDF $f_e(v_{k\theta 1})$ gives $T_{ek\theta 1} = \cos^2\theta T_{e\perp} + \sin^2\theta T_{e||}$, and the corresponding electron thermal velocity $V_{tek\theta 1}$ is plotted as the curved white line in Fig. 3(b). Interestingly, this line does not exactly follow any contour line for $F_e(v_x,v_z)$. Therefore, for $V_{k||1}$ and $V_{k||2}$ in our system, $\theta = 45°$ and $135°$, the parallel electron temperature can be written as,

$$T_{e||} = 2T_{ek||1,2} - T_{e\perp}. \tag{3}$$

Based on Eq. (1) and (3), $T_{e||}$ and the electron temperature anisotropy $T_{e||}/T_{e\perp}$ are calculated as a function of $T_{ek\perp}$ and $T_{ek||}$ and are presented as black solid lines and contours in Fig. 3(c). Isotropic electron distributions are located in the green shaded region around the green dashed line which includes a 10% electron temperature measurement uncertainty.

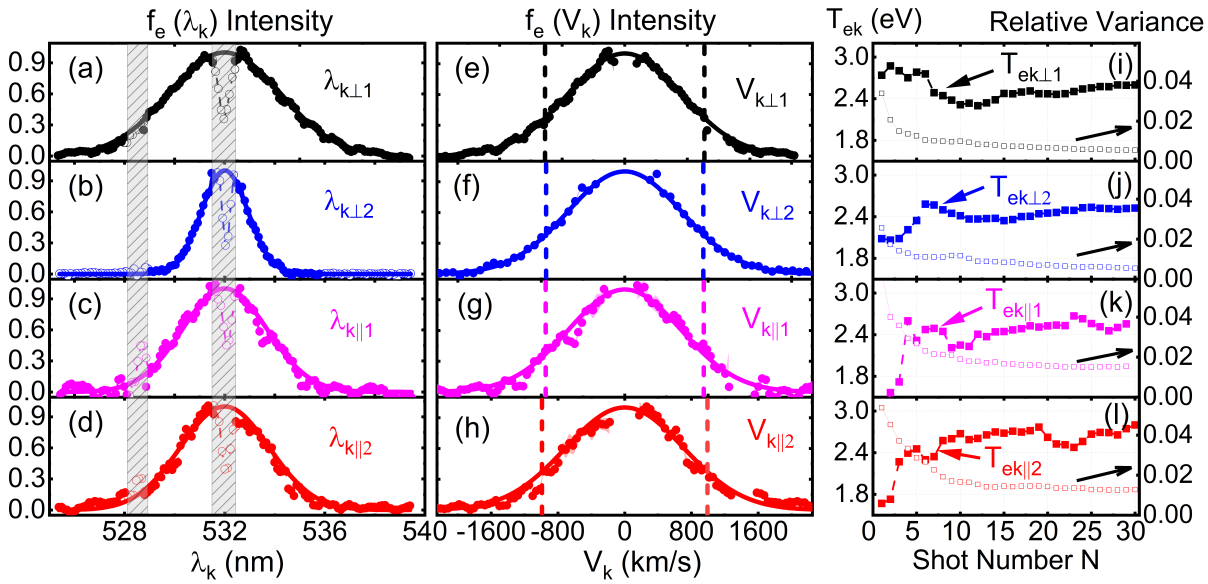

FIG. 4. (a-d) Measured Thomson scattering spectra $f_e(\lambda_{k\perp 1})$, $f_e(\lambda_{k\perp 2})$, $f_e(\lambda_{k\|1})$ and $f_e(\lambda_{k\|2})$ of the single magnetic flux rope plasma. Solid circles are points used for fittings whose results are plotted in solid lines. Gray shaded areas denote cutoff regions. (e-h) EVDFs $f_e(v_{k\perp 1})$, $f_e(v_{k\perp 2})$, $f_e(v_{k\|1})$ and $f_e(v_{k\|2})$ and fitted electron thermal speeds are shown by vertical dashed lines. (i-l) The dependence of fitted electron temperatures $T_{ek\perp 1}$, $T_{ek\perp 2}$, $T_{ek\|1}$, $T_{ek\|2}$ and their relative variance of spectra intensity on the accumulated shot number N.

III. MUTLI-DIMENSIONAL EVDFS

A. Magnetic Flux Rope

Benchmark measurements with this multi-dimensional Thomson scattering system were performed on a plasma expected to exhibit thermal isotropy. An isotropic plasma was chosen to demonstrate consistency between the velocity distributions independently measured along the four different velocity axes. In other words, any observed differences provide a measure of the uncertainty in the different EVDF measurements. The plasma case selected was a kink-free magnetic flux rope plasma formed by single plasma gun in PHASMA.[28] An isotropic 3D EVDF is expected because no special electron energization processes are anticipated and because the characteristic time for isotropization between $T_{e\|}$ and $T_{e\perp}$, $\leqslant 0.1\mu$s, is small compared to the timescale for global plasma motion and the characteristic isotropization length, 0.1 m, is much less than the flux rope length of 1 m.

Figure 4 (a-d) show four Thomson scattering spectra $f_e(\lambda_{k\perp 1})$, $f_e(\lambda_{k\perp 2})$, $f_e(\lambda_{k\|1})$ and $f_e(\lambda_{k\|2})$ measured along $\mathbf{k}_{\perp\mathbf{1}}$, $\mathbf{k}_{\perp\mathbf{2}}$, $\mathbf{k}_{\|\mathbf{1}}$ and $\mathbf{k}_{\|\mathbf{2}}$, at a radial location of 20 mm from the center of the single flux rope plasma. Compared to previously obtained Thomson scattering spectra,[9,17] the measured wavelength range is much larger since the new spectrometer has a shorter focal length and a larger linear dispersion. These two wavelength regions, indicated by the gray shaded areas, are excluded from analysis. The region around the laser wavelength of $\lambda_k = 532$ nm is excluded because notch filters are used and spectra are artificially suppressed. There is a strong impurity line from Fe I around 528.5 nm and that region of the collected spectra is also excluded. The remaining spectral intensity measurements (solid circles) are fitted to Maxwellian profiles as shown by the solid lines. The noticeably different spectral widths result from the different lengths of the scattering wavevectors shown in Fig. 2.

The Thomson scattering spectra on the λ_k axes are converted to EVDFs in velocity V_k space in Fig. 4 (e-h), $V_k = -c(\lambda_k - \lambda_i)/[2\lambda_i \sin(\theta_s/2)]$, where c is the speed of light in vacuum. The electron thermal velocities obtained from Maxwellian fits are plotted as vertical dashed lines on each spectrum. Note that in velocity space, the electron thermal velocities of $f_e(v_{k\perp 1})$ and $f_e(v_{k\perp 2})$ are nearly identical, even though each was measured with scattering wavevectors of different magnitudes. The gyrotropicity of the EVDF is consistent with expectations given the strong magnetization of the electrons. Nearly equal electron thermal velocities are also obtained from the two parallel injection measurements, $f_e(v_{k\|1})$ and $f_e(v_{k\|2})$. These nearly identical results arise from the symmetric layout of the two collection paths relative to the parallel injection direction.

The same methods for determining electron temperature and temperature measurement uncertainty used in our previous work[17] are applied to each of four spectra. The spectra are accumulated for 30 repeatable discharges to obtain one EVDF in these experiments. Based on the spectrum accumulated in the first N shots, the electron temperature is derived from Maxwellian fits and the relative variance is calculated from the deviation between the measured Thomson scattering spectrum and fitted Maxwellian spectrum (the solid squares and open circles in Fig. 4 (i-l)). After the relative variance curve settles down to a gradually changing values and the magnitude of the variance drops below 2%, $N = 10$ shots for these experiments, the electron temperature (the mean) and

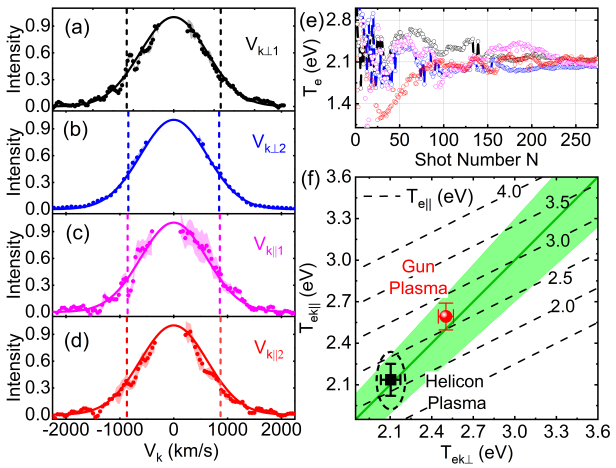

FIG. 5. (a-d) Measured EVDFs in a helicon plasma $f_e(v_{k\perp1})$, $f_e(v_{k\perp2})$, $f_e(v_{k\parallel1})$ and $f_e(v_{k\parallel2})$. Solid circles are points used for fits. The fit results are shown by solid lines with corresponding electron thermal velocities denoted by vertical dashed lines. (e) The electron temperatures from fits to the EVDFs accumulated for the first N shots. (f) The black square shows the measured $T_{ek\perp}$ and $T_{ek\parallel}$ of the helicon plasma while the red circle is for measurements obtained in the single magnetic flux rope. Dashed lines indicate derived $T_{e\parallel}$ values. The isotropic region is denoted by the green shading, which includes a 10% measurement uncertainty.

the temperature error (the standard deviation) are calculated. $T_{ek\perp1} = 2.5 \pm 0.1$ eV, $T_{ek\perp2} = 2.5 \pm 0.1$ eV, $T_{ek\parallel1} = 2.5 \pm 0.1$ eV and $T_{ek\parallel2} = 2.6 \pm 0.1$ eV. Thus, the parallel electron temperature $T_{e\parallel} = 2.7 \pm 0.2$ eV and the anisotropy, if any, in the electron temperature is very small, i.e., $T_{e\parallel}/T_{e\perp} = 1.1 \pm 0.1$. These isoptropic measurements confirm the isotropic nature of the single magnetic flux rope plasma.

B. Helicon Plasma

In addition to pulsed single magnetic flux rope case, isotropic steady-state helicon plasmas were also used to validate the 3D Thomson scattering system. Since the axial location of the Thomson scattering spectra measurements is 2 m downstream of the helicon antenna, the electron density $10^{17-18}\mathrm{m}^{-3}$ and electron temperature ~ 2 eV is much lower than in the single flux rope studies. Here again, the plasma is expected to be isotropic given the large electron-electron collision frequency, significant electron-neutral collisions, and the lack of physical process that energizes a specific component of the EVDF.

Figure 5 (a-d) present $f_e(v_{k\perp1})$, $f_e(v_{k\perp2})$, $f_e(v_{k\parallel1})$ and $f_e(v_{k\parallel2})$ measured for a helicon plasma for an input radio frequency power of 800 W and a background neutral pressure of 8 mTorr (fairly large for a helicon plasma). More shots, $N = 275$, are accumulated into one spectrum because the electron density is much smaller than in the magnetic flux rope plasmas. Another difference is that no strong Fe I emission line is observed as there are no physical contacts between plasmas and electrodes to introduce impurities. The electron thermal velocities obtained from Maxwellian fits are very close to each other. From Fig. 5 (e), we find $T_{ek\perp1} = 2.2 \pm 0.1$ eV, $T_{ek\perp2} = 2.1 \pm 0.1$ eV, $T_{ek\parallel1} = 2.2 \pm 0.1$ eV and $T_{ek\parallel2} = 2.1 \pm 0.1$ eV. As is shown by the black square point in Fig. 5 (f), $T_{e\parallel} = 2.2 \pm 0.2$ eV and $T_{e\parallel}/T_{e\perp} = 1.0 \pm 0.1$. The anisotropy measurement obtained in the magnetic flux rope plasma is indicated by the red circle. Both measurements are well within the isotropic EVDF region (the green shaded region), consistent with expectations for isotropic plasmas.

IV. SUMMARY

In summary, a first-of-its-kind multi-dimensional incoherent Thomson scattering diagnostic system has been implemented on the PHASMA facility. Two injection paths (perpendicular and parallel to the axial direction) and two collection paths (opposite each other along a common radial chord) provide four independent EVDF measurements along four different velocity directions. These four measured EVDFs can be used to reconstruct the 3D EVDFs of strongly magnetized electrons through the assumption of gyrotropicity. The result is two characteristic electron temperature $T_{e\parallel}$ and $T_{e\perp}$ (perpendicular and parallel to z). The reconstruction is over determined, so there is inherent validity test with each 3D measurement. To validate this system, EVDFs of isotropic electrons in both pulsed single magnetic flux rope plasmas and steady-state helicon plasmas were measured. In both cases, the measurements confirmed the expected isotropic nature of the target plasmas. In future experiments, *e.g.*, magnetic reconnection between two interacting magnetic flux ropes[29] and during low-pressure helicon wave damping studies,[30] 3D EVDF measurements are expected to provide important insight into the electron energization mechanisms that lead to the electron temperature anisotropy.

ACKNOWLEDGMENTS

This work is supported by NSF awards PHY 1827325 and 1902111 and DoE Award DE-SC0020294. The authors would like to thank Prabhakar Srivastav, Thomas Steinberger and Sonu Yadav of West Virgina University for their technical help with commissioning pulsed laser sources.

DATA AVAILABILITY

The data that support the findings of this study are available from the corresponding author upon reasonable requests.

[1] V. Godyak, IEEE Transactions on Plasma Science **34**, 755 (2006).
[2] G. G. Howes, Physics of Plasmas **25**, 055501 (2018).
[3] V. Kolobov and V. Godyak, Physics of Plasmas **26**, 060601 (2019).
[4] S. D. Bale, J. C. Kasper, G. G. Howes, E. Quataert, C. Salem, and D. Sundkvist, Physical Review Letters **103**, 211101 (2009).
[5] X. Li, F. Guo, and Y.-H. Liu, Physics of Plasmas **28**, 052905 (2021).
[6] H. Ji, W. Daughton, J. Jara-Almonte, A. Le, A. Stanier, and J. Yoo, Nature Reviews Physics **4**, 263 (2022).
[7] J. W. R. Schroeder, G. G. Howes, C. A. Kletzing, F. Skiff, T. A. Carter, S. Vincena, and S. Dorfman, Nature Communications **12**, 3103 (2021).

[8]F. Taccogna and G. Dilecce, The European Physical Journal D **70**, 251 (2016).
[9]P. Shi, P. Srivastav, M. H. Barbhuiya, P. A. Cassak, E. E. Scime, and M. Swisdak, Physical Review Letters **128**, 025002 (2022).
[10]I. D. Kaganovich, A. Smolyakov, Y. Raitses, E. Ahedo, I. G. Mikellides, B. Jorns, F. Taccogna, R. Gueroult, S. Tsikata, A. Bourdon, J.-P. Boeuf, M. Keidar, A. T. Powis, M. Merino, M. Cappelli, K. Hara, J. A. Carlsson, N. J. Fisch, P. Chabert, I. Schweigert, T. Lafleur, K. Matyash, A. V. Khrabrov, R. W. Boswell, and A. Fruchtman, Physics of Plasmas **27**, 120601 (2020).
[11]P. V. Savrukhin, Physical Review Letters **86**, 3036 (2001).
[12]Y. Liu, P. Shi, X. Zhang, J. Lei, and W. Ding, Review of Scientific Instruments **92**, 71101 (2021).
[13]R. L. Stenzel and J. M. Urrutia, Review of Scientific Instruments **92**, 111101 (2021).
[14]W. Gekelman and R. L. Stenzel, Physical Review Letters **54**, 2414 (1985).
[15]D. Dodt, A. Dinklage, R. Fischer, K. Bartschat, O. Zatsarinny, and D. Loffhagen, Journal of Physics D: Applied Physics **41**, 205207 (2008).
[16]A. M. DuBois, A. F. Almagri, J. K. Anderson, D. J. Den Hartog, J. D. Lee, and J. S. Sarff, Physical Review Letters **118**, 075001 (2017).
[17]P. Shi, P. Srivastav, C. Beatty, R. S. Nirwan, and E. E. Scime, Review of Scientific Instruments **92**, 033102 (2021).
[18]S. Ghazaryan, M. Kaloyan, W. Gekelman, Z. Lucky, S. Vincena, S. K. P. Tripathi, P. Pribyl, and C. Niemann, Review of Scientific Instruments **93**, 083514 (2022).
[19]M. Xu, Q. Zhang, and J. Xie, Plasma Science and Technology **24**, 064008 (2022).
[20]R. Agnello, Y. Andrebe, H. Arnichand, P. Blanchard, T. De Kerchove, I. Furno, A. A. Howling, R. Jacquier, and A. Sublet, Journal of Plasma Physics **86**, 905860306 (2020).
[21]A. L. Milder, J. Katz, R. Boni, J. P. Palastro, M. Sherlock, W. Rozmus, and D. H. Froula, Physics of Plasmas **28**, 082102 (2021).
[22]P. Shi, P. Srivastav, C. Beatty, R. John, M. Lazo, J. McKee, J. McLaughlin, M. Moran, M. Paul, E. E. Scime, E. E. Scime, D. Thompson, and T. Steinberger, Physics of Plasmas **28**, 032101 (2021).
[23]K. Stevenson, T. N. Good, T. J. Gilbert, P. Srivastava, M. C. Paul, P. Shi, T. E. Teinberger, R. S. Nirwan, and E. E. Scime, Plasma Sources Science and Technology , *to be submitted* (2022).
[24]M. C. Paul and E. E. Scime, Review of Scientific Instruments **92**, 043532 (2021).
[25]T. J. Gilbert, K. J. Stevenson, M. C. Paul, T. E. Steinberger, and E. E. Scime, AIP Advances **11**, 055314 (2021).
[26]B. Vincent, S. Tsikata, S. Mazouffre, T. Minea, and J. Fils, Plasma Sources Science and Technology **27**, 055002 (2018).
[27]J. Sheffield, D. Froula, S. H. Glenzer, and N. C. Luhmann, *Plasma Scattering of Electromagnetic Radiation: Theory and Measurement Techniques* (Academic Press, 2010) p. 73.
[28]P. Shi, P. Srivastav, M. H. Barbhuiya, P. A. Cassak, E. E. Scime, M. Swisdak, C. Beatty, T. Gilbert, R. John, M. Lazo, R. S. Nirwan, M. Paul, E. E. Scime, K. Stevenson, and T. Steinberger, Physics of Plasmas **29**, 032101 (2022).
[29]L. Franci, E. Papini, A. Micera, G. Lapenta, P. Hellinger, D. D. Sarto, D. Burgess, and S. Landi, The Astrophysical Journal **936**, 27 (2022).
[30]E. M. Aguirre, R. Bodin, N. Yin, T. N. Good, and E. E. Scime, Physics of Plasmas **27**, 123501 (2020).